iScience

CellPress
OPEN ACCESS

Article

Bubble Formation in the Electrolyte Triggers Voltage Instability in CO_2 Electrolyzers

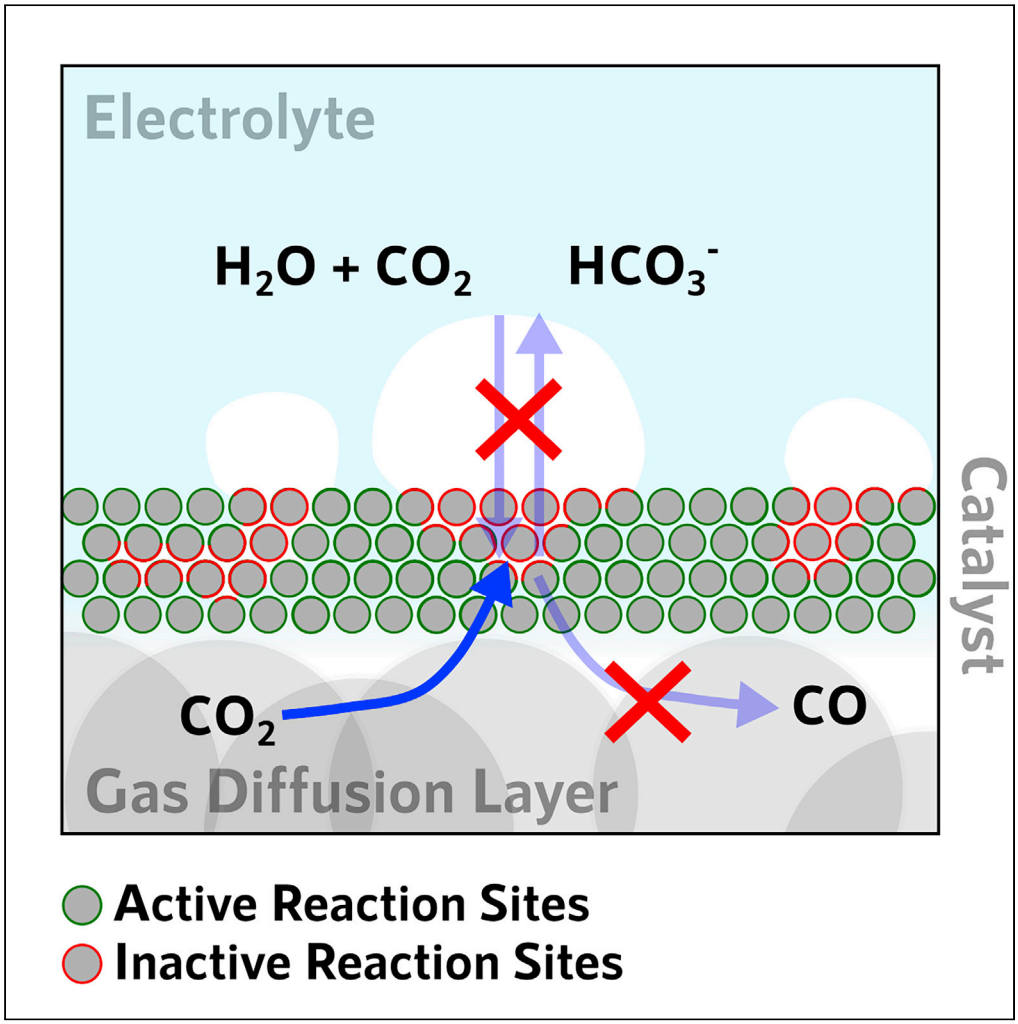

ChungHyuk Lee, Benzhong Zhao, Jason K. Lee, Kieran F. Fahy, Kevin Krause, Aimy Bazylak

abazylak@mie.utoronto.ca

HIGHLIGHTS

X-ray imaging was used to characterize the bubble formation in a CO_2 electrolyzer

Gas formed near the GDE-electrolyte chamber interface and caused voltage instabilities

We hypothesize that gas physically inhibits two-phase reaction interfaces

Lee et al., iScience *23*, 101094
May 22, 2020
https://doi.org/10.1016/j.isci.2020.101094

iScience

CellPress
OPEN ACCESS

Article

Bubble Formation in the Electrolyte Triggers Voltage Instability in CO_2 Electrolyzers

ChungHyuk Lee,[1] Benzhong Zhao,[1,2] Jason K. Lee,[1] Kieran F. Fahy,[1] Kevin Krause,[1] and Aimy Bazylak[1,3,*]

SUMMARY

The electrochemical reduction of CO_2 is promising for mitigating anthropogenic greenhouse gas emissions; however, voltage instabilities currently inhibit reaching high current densities that are prerequisite for commercialization. Here, for the first time, we elucidate that product gaseous bubble accumulation on the electrode/electrolyte interface is the direct cause of the voltage instability in CO_2 electrolyzers. Although bubble formation in water electrolyzers has been extensively studied, we identified that voltage instability caused by bubble formation is unique to CO_2 electrolyzers. The appearance of syngas bubbles within the electrolyte at the gas diffusion electrode (GDE)-electrolyte chamber interface (i.e. ~10% bubble coverage of the GDE surface) was accompanied by voltage oscillations of 60 mV. The presence of syngas in the electrolyte chamber physically inhibited two-phase reaction interfaces, thereby resulting in unstable cell performance. The strategic incorporation of our insights on bubble growth behavior and voltage instability is vital for designing commercially relevant CO_2 electrolyzers.

INTRODUCTION

Global CO_2 emissions from fossil fuel consumption continue to grow despite significant advancements in clean energy technologies (Peters et al., 2020). The demand for electricity far exceeds the rate of clean energy technology implementation, consequently leading to a net increase in fossil-fuel-sourced CO_2 emissions (York, 2012). Clean energy technologies that lessen societal dependence on fossil fuels are needed to accelerate the necessary transition from a carbon-based energy infrastructure to a clean-energy-based infrastructure.

The electrochemical conversion of CO_2 to useful chemical products (e.g. CO and HCOOH) is a promising means to realize this transition to a carbon neutral energy infrastructure (Bushuyev et al., 2018; Smith et al., 2019). By utilizing fuels generated via CO_2 electrolyzers that are powered by renewable energy, carbon neutral transportation can be achieved (Smith et al., 2019). In recent years, there has been a significant growth in research activities focused on developing next-generation catalysts and membranes for enhanced selectivity toward carbon-based chemical products for CO_2 reduction (Dinh et al., 2018; Gallo et al., 2019; García de Arquer et al., 2020; Li et al., 2020; Verma et al., 2018; Vermaas and Smith, 2016; Zheng et al., 2019). Although these pioneering works have illustrated the promise of CO_2 electrolysis, there are major challenges associated with commercially relevant operating conditions, such as achieving high current densities (i.e. $i > 200$ mA/cm^2), which have remained largely overlooked (Burdyny and Smith, 2019; Smith et al., 2019; Weekes et al., 2018).

The operation of CO_2 electrolyzers at elevated current densities has been accompanied by unfavorable conditions, such as increased electrolyte pH near the catalyst surface (Burdyny and Smith, 2019; Ma et al., 2020; Singh et al., 2017) and unstable cathodic overvoltage (Nwabara et al., 2019; Verma et al., 2018). In particular, previous studies have shown that unstable cathodic overvoltages directly limit the high current density operation of CO_2 electrolyzers (Gabardo et al., 2019; Kuhl et al., 2012; Sen et al., 2019), yet the direct cause of this instability remains unclear. One proposed cause is salt precipitation within the liquid electrolyte adjacent to the membrane and gas diffusion electrode (GDE) (Dufek et al., 2012; Schulz et al., 2006). Recently, Nwabara et al. (Nwabara et al., 2019) demonstrated that the increase in cell voltage due to salt precipitation is partially recoverable with a flowing electrolyte. Another proposed cause of this voltage instability is the formation of gaseous species within the electrolyte, which physically

[1]Thermofluids for Energy and Advanced Materials Laboratory, Department of Mechanical and Industrial Engineering, Institute for Sustainable Energy, Faculty of Applied Science and Engineering, University of Toronto, 5 King's College Road, Toronto, ON M5S 3G8, Canada

[2]Department of Civil Engineering, McMaster University, Hamilton, ON, L8S 4L7, Canada

[3]Lead Contact

*Correspondence: abazylak@mie.utoronto.ca

https://doi.org/10.1016/j.isci.2020.101094

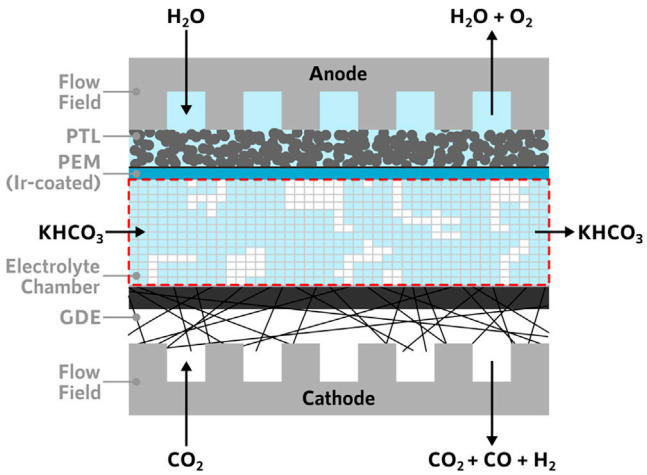

Figure 1. Schematic of the CO_2 Electrolyzer Cell Used in This Work

The electrolyte chamber was packed with high-density polyethylene (HDPE) meshes to provide structural support to the proton exchange membrane (PEM) and the silver-based gas diffusion electrode (GDE). Gas bubbles (white) are shown within the electrolyte chamber. The red-dashed box indicates the region of interest that was captured via synchrotron X-ray imaging.

blocks the reaction sites (Kuhl et al., 2012; Nwabara et al., 2019; Sen et al., 2019). When the GDE is not sufficiently porous for product gas diffusion, this product gas may accumulate within the electrolyte chamber (Nwabara et al., 2019). Although bubble-induced electrochemical losses have been identified by previous works (Angulo et al., 2020), there is a complete absence in the literature of any direct evidence of this gas accumulation and its effect on the cell voltage. Understanding the complex two-phase transport within the electrolyte chamber is a necessary first step in designing next-generation CO_2 electrolyzers capable of operating at commercially relevant conditions.

Here, we directly visualized gas bubble formation within the electrolyte chamber via *in operando* synchrotron X-ray imaging with high spatial (6.5 um/pixel) and temporal (1 s per frame) resolution imaging (Lee et al., 2020). We performed the experiments at the Biomedical Imaging and Therapy Wiggler Insertion Device beamline at the Canadian Light Source (CLS) in Saskatoon, Canada (Wysokinski et al., 2013). The CO_2 electrolyzer was custom designed to constrain the X-ray attenuation to the active area of the cell. A flow cell configuration with a liquid electrolyte chamber was used in this work. Although liquid electrolyte chambers have been used in similar cell configurations by other authors (Delacourt et al., 2008; Gabardo et al., 2019; Liu et al., 2019), a major distinguishing feature of our unique design is that our electrolyte chamber was packed with high-density polyethylene (HDPE) meshes to provide structural support to the proton exchange membrane (PEM) and the GDE for high-resolution synchrotron X-ray imaging (see Figure 1). Stabilizing the membrane is based on our previous imaging work of electrochemical cell designs (Banerjee et al., 2018; Chevalier et al., 2017; Ge et al., 2019). We supplied deionized water at 10 mL/min to the anode flow field, aqueous $KHCO_3$ (0.5 M) at 6 mL/min to the electrolyte chamber, and dry CO_2 gas at 100 mL/min to the cathode flow field. The GDE was coated with a silver catalyst, which was chosen for its high selectivity toward CO generation (Martín et al., 2015). For details, the readers are referred to the Methods section.

RESULTS AND DISCUSSION

Characteristics of Bubble Formation within the Electrolyte Chamber

The results of imaging the electrolyte chamber are presented in Figure 2. We assumed two gases that were formed within the electrolyte chamber: (1) CO_2, which preferentially formed near the PEM-electrolyte chamber interface and (2) a mixture of CO and H_2 (i.e. syngas), which preferentially formed near the electrolyte chamber-GDE interface. The presence of these gases within the electrolyte chamber can be validated via performing gas chromatography (GC) on the gaseous products exiting the electrolyte chamber. At the PEM-electrolyte chamber interface (the upper region of each image in Figure 2), the following reaction drove the production of CO_2 gas:

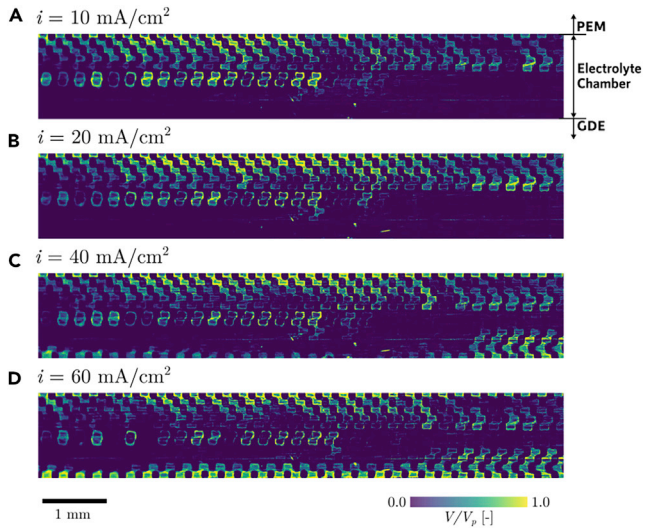

Figure 2. Processed Images of the Electrolyte Chamber

Images are taken at 1 frame per second during steady-state operation of the CO_2 electrolyzer at current densities of (A) 10 mA/cm^2, (B) 20 mA/cm^2, (C) 40 mA/cm^2, and (D) 60 mA/cm^2. The images correspond to the spatial distribution of gas saturation (averaged over the last 100 frames of each experiment) within the electrolyte chamber. The upper region of each image corresponds to the interface between the electrolyte chamber and the PEM, whereas the lower region corresponds to the interface between the electrolyte chamber and the GDE. As a result, the gas clusters in the upper region corresponded to CO_2 gas, whereas the gas clusters in the lower region corresponded to syngas.

$$H^+ + HCO_3^- \rightarrow H_2O + CO_2 \qquad \text{(Equation 1)}$$

At the GDE-electrolyte chamber interface (the lower region of each image in Figure 2), the CO_2 reduction reaction (CO_2RR) and hydrogen evolution reaction (HER) drove the formation of syngas. Surprisingly, we observed a contrasting trend between the syngas accumulation behavior near the GDE-electrolyte chamber interface and CO_2 accumulation behavior near the PEM-electrolyte chamber interface. Specifically, syngas was not observed in the electrolyte chamber until a critical current density of i = 40 mA/cm^2 was reached (Figure 2C), in contrast to the appearance of CO_2 gas in the electrolyte chamber, which was visible when i = 10 mA/cm^2 (Figure 2A).

To obtain further insight into the product gas accumulation behavior, we divided the electrolyte chamber into three regions of equal thickness: PEM interface region, bulk region, and GDE interface region (Figure 3A). As current density was increased, the gas saturation in the PEM interface region decreased, whereas the gas saturation near the GDE interface region sharply increased (Figure 3B). Specifically, the gas saturation in the PEM interface region decreased from 0.255 (at i = 20 mA/cm^2) to 0.193 (at i = 60 mA/cm^2), whereas the saturation in the GDE interface region increased from 0.009 (at i = 20 mA/cm^2) to 0.217 (at i = 60 mA/cm^2). The decrease in gas accumulation in the PEM interface region at higher current densities was attributed to more frequent bubble detachment from the PEM interface region (Figure 4A). We observed less frequent bubble detachment at lower current densities (~0.07 s^{-1} at i = 20 mA/cm^2, Figure 4A and see also Video S2) compared with the frequency of bubble detachment in the PEM interface region at high current densities (~0.27 s^{-1} at i = 60 mA/cm^2, Figure 4A and see also Video S4). More frequent removal of gas from the PEM interface region led to lower average gas saturation at the PEM interface region.

The sharp increase in the gas saturation (increase of 0.208) at the GDE interface region with increasing current density was attributed to the porous nature of the GDE surface. Product syngas entered the electrolyte chamber and the GDE (depending on the porous structure of the GDE (Nwabara et al., 2019)). Thus, we hypothesized that at low current densities (i.e. $i \leq$ 20 mA/cm^2), the majority of the generated syngas diffused into the GDE, and a further increase in current density promoted bubble formation in the electrolyte chamber. We further supported our hypothesis by comparing the trends in syngas evolution in the GDE interface region (Figure 4B) with that in the CO_2 evolution in the PEM interface region (Figure 4A). The gas

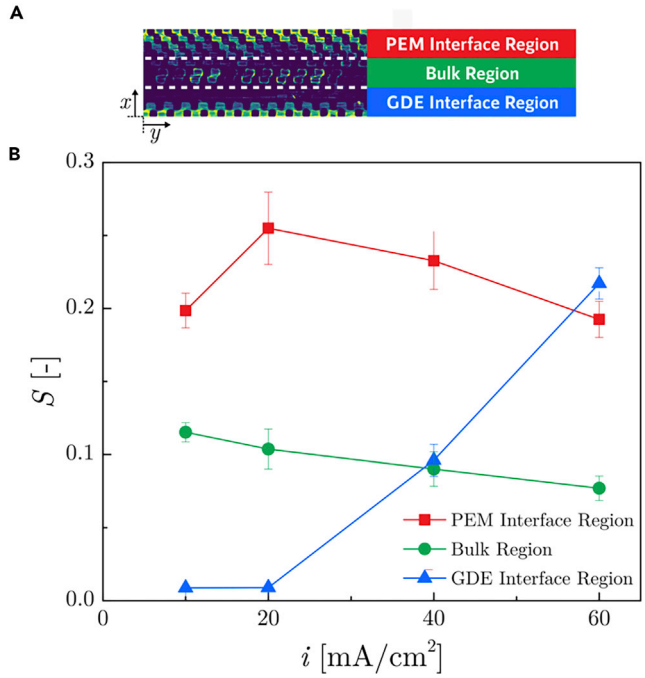

Figure 3. Average Gas Saturation in Three Distinct Regions of the Electrolyte Chamber

(A) Three regions in the electrolyte chamber were defined to calculate the local average gas saturation. The electrolyte chamber was divided into regions of equal thickness: the *PEM Interface Region* refers to the upper region immediately adjacent to the PEM, the *Bulk Region* refers to the region in the center of the electrolyte chamber, and the *GDE Interface Region* refers to the lower region immediately adjacent to the GDE.

(B) The resulting average gas saturation in each region. The error bars show one standard deviation of 100 images that were averaged for each data point. We observed a decrease in average gas saturation in the PEM interface region and a sharp increase in the GDE interface region with increasing current density.

generated within the electrolyte layer in the GDE interface region exhibited a unique behavior compared with the gas generated in the PEM interface region (Figures 4A and 4B and see also Videos S1, S2, S3, and S4). For the CO_2 gas that accumulated in the PEM interface region, we observed a sequence of bubble growth and detachment (Figure 4A). On the other hand, the accumulation of syngas in the GDE interface region exhibited a relatively smooth profile (Figure 4B), implying that syngas entered not only the electrolyte chamber but also the porous GDE. The majority of the syngas exited via the porous GDE; therefore, the volumetric growth rate of syngas bubbles in the electrolyte chamber was relatively slow compared with the CO_2 bubbles in the PEM interface region.

Voltage Instability Caused by Bubble Formation

We observed a strong correlation between the bubble accumulation behavior at the electrolyte-GDE interface and the stability of the cell voltage. Specifically, unstable cell voltages were observed with the simultaneous accumulation of syngas in the GDE region of the electrolyte at a critical current density (i.e. i = 40 mA/cm^2) (Figure 5A). The standard deviations in the cell voltage were 0.00, 0.00, 0.01, 0.06, 0.22, and 0.38 V for current densities of 5, 10, 20, 40, 60, and 80 mA/cm^2 (shown in Figure 5A). CO_2 bubbles were detected in the PEM interface region when $i \leq 20$ mA/cm^2, but this gas accumulation did not influence the voltage stability. The dynamic CO_2 bubble generation in the PEM region may have influenced the overall two-phase transport behavior within the electrolyte chamber; however, the presence of syngas bubbles in the GDE region exhibited the most significant impact on unstable cell voltages.

The strong correlation between bubble formation on the GDE-electrolyte chamber interface and the cell voltage stability was attributed to the physical break of the two-phase reaction interface (Figures 5B and 5C). The reaction sites for syngas generation exist at the interface between the catalyst particles and the liquid electrolyte with dissolved CO_2 as the main reagent (the interface is highlighted in green in Figure 5B)

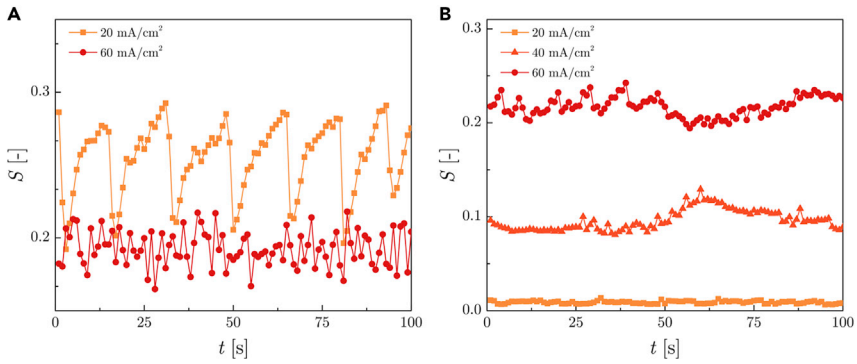

Figure 4. Evolution in Local Gas Saturations

Gas evolution within (A) the PEM interface region and (B) the GDE interface region. The gas evolution behavior in the PEM interface region exhibited sequence of growth and detachment, whereas that in the GDE interface region exhibited a smooth and relatively slower growth.

(Burdyny and Smith, 2019). However, as syngas bubbles formed on the GDE-electrolyte chamber interface, the two-phase reaction boundaries became physically separated in the presence of syngas bubbles, temporarily reducing the total active reaction site area (Figure 5C). The relatively slow growth and detachment of syngas bubbles led to undesired reaction site blockage, which manifested as an unstable cell voltage.

Conclusion

Here, we directly observed unique bubble accumulation behavior within the liquid electrolyte chamber of a flow-cell-based CO_2 electrolyzer, and we explained how this behavior leads to undesired cell voltage instabilities. CO_2 and syngas bubbles accumulated in the PEM interface region and the GDE interface region, respectively, and these regions exhibited contrasting growth and accumulation behavior. Specifically, CO_2 bubbles exhibited a two-stage (i.e. growth and detachment) behavior with a frequency $<< 1\ s^{-1}$ from the onset current density, whereas significantly less frequent syngas bubble growth and detachment events were observed, only appearing when $i \geq 40\ mA/cm^2$. The appearance of these syngas bubbles was accompanied by an undesired fluctuation in cell voltage, where the standard deviation suddenly escalated up to 60 mV at $i = 40\ mA/cm^2$. We attributed this instability in cell voltage to the temporary blockage of the two-

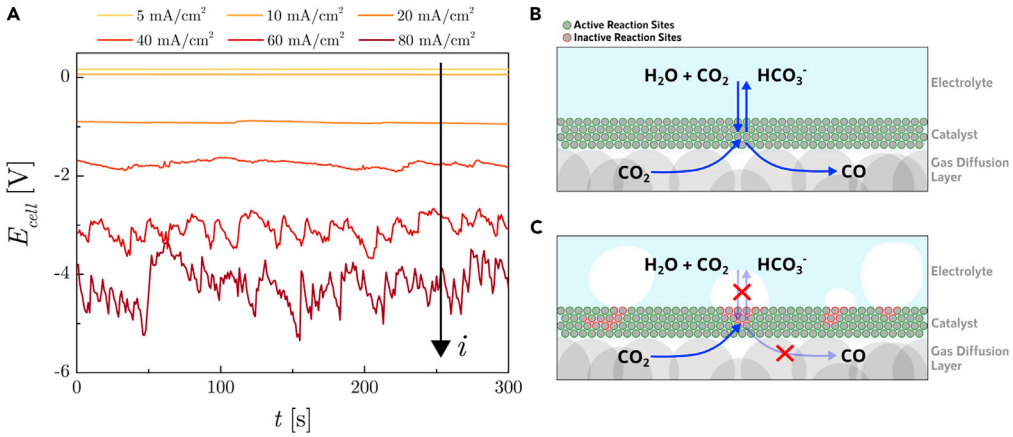

Figure 5. Cell Voltage Instability Caused by Gas Accumulation in the GDE Interface Region

(A) Transient response in cell voltage with increasing current density, indicated by the arrow. The cell voltage was measured every second, and we present the last 300 s of each current density operation.

(B and C) Schematics of the catalyst layer reaction sites (B) in the absence of gas and (C) with the presence of gas. The presence of gas physically impeded the two-phase reaction interface (i.e. interface between the liquid electrolyte with dissolved CO_2 and catalyst particles), resulting in a temporary decrease in cell voltage.

phase reaction interface between the catalyst and the CO_2-dissolved electrolyte. Our results inform the importance of mitigating bubble coverage of the GDE-electrolyte chamber interface, which is vital for achieving commercially relevant operating conditions of CO_2 electrolyzers. Therefore, we recommend future work to mitigate bubble accumulation in the electrolyte chamber: (1) design new porous GDEs or electrolyte chambers that promote product transport into the GDE and (2) tailor the liquid electrolyte and gaseous CO_2 flow rates to maximize the two-phase reaction interface areas.

Limitations of the Study

This work presents experimental evidence of the severe effects of bubble formation within the electrolyte chamber on cell voltage, and further investigations may be undertaken to extend our results to different experimental set-ups. Specifically, the addition of HDPE meshes into the electrolyte chamber was primarily for preventing the movement of the GDE and PEM during imaging, but these meshes may potentially encourage gas accumulation near the GDE interface region. Additionally, the type of GDE used in this work, although commercial, may have promoted bubble formation in the electrolyte chamber rather than product transport toward the cathode flow field due to its porous microstructure. Additional experiments with varied GDE structures are crucial for elucidating optimal GDE structures for enhanced transport. Lastly, the CO_2 gas flow rate and electrolyte flow rate were held constant throughout the experiment; varying these parameters is also necessary for identifying the dependence of the bubble effects on the prescribed flow conditions.

METHODS

All methods can be found in the accompanying Transparent Methods supplemental file.

DATA AND CODE AVAILABILITY

The imaging data that support the figures and plots in this work are available from the lead contact upon reasonable request.

SUPPLEMENTAL INFORMATION

Supplemental Information can be found online at https://doi.org/10.1016/j.isci.2020.101094.

ACKNOWLEDGMENTS

Financial support from the Natural Sciences and Engineering Research Council of Canada (NSERC) and the Canada Research Chairs Program are gratefully acknowledged. Research described in this paper was performed at the BMIT facility at the Canadian Light Source, which is supported by the Canada Foundation for Innovation, Natural Sciences and Engineering Research Council of Canada, the University of Saskatchewan, the Government of Saskatchewan, Western Economic Diversification Canada, the National Research Council Canada, and the Canadian Institutes of Health Research. Authors acknowledge the receipt of support from the CLS Post-Doctoral and Graduate Student Travel Support Program. The authors would like to acknowledge Denise Miller, Sergey Gasilov, Ning Zhu, Adam Webb, and the BMIT group of the Canadian Light Source for their generous assistance.

AUTHOR CONTRIBUTIONS

CH. L. and B. Z. designed the hardware and experiments, carried out all experiments, and prepared the manuscript. J. K. L. and K. F. F. assisted with the experimental setup and execution of the experiments. A. B. defined the experimental approach, supervised, and funded the project. All authors contributed to the discussion and analysis of the data, as well as the editing of the manuscript.

DECLARATION OF INTERESTS

The authors declare no competing interests.

Received: March 14, 2020
Revised: April 13, 2020
Accepted: April 17, 2020
Published: May 22, 2020

REFERENCES

Angulo, A., van der Linde, P., Gardeniers, H., Modestino, M., and Fernández Rivas, D. (2020). Influence of bubbles on the energy conversion efficiency of electrochemical reactors. Joule *4*, 555–579.

Banerjee, R., Ge, N., Han, C., Lee, J., George, M.G., Liu, H., Muirhead, D., Shrestha, P., and Bazylak, A. (2018). Identifying in operando changes in membrane hydration in polymer electrolyte membrane fuel cells using synchrotron X-ray radiography. Int. J. Hydrogen Energy *43*, 9757–9769.

Burdyny, T., and Smith, W.A. (2019). CO2 reduction on gas-diffusion electrodes and why catalytic performance must be assessed at commercially-relevant conditions. Energy Environ. Sci. *12*, 1442–1453.

Bushuyev, O.S., De Luna, P., Dinh, C.T., Tao, L., Saur, G., van de Lagemaat, J., Kelley, S.O., and Sargent, E.H. (2018). What should we make with CO2 and how can we make it? Joule *2*, 825–832.

Chevalier, S., Ge, N., Lee, J., George, M.G., Liu, H., Shrestha, P., Muirhead, D., Lavielle, N., Hatton, B.D., and Bazylak, A. (2017). Novel electrospun gas diffusion layers for polymer electrolyte membrane fuel cells: Part II. In operando synchrotron imaging for microscale liquid water transport characterization. J. Power Sources *352*, 281–290.

Delacourt, C., Ridgway, P.L., Kerr, J.B., and Newman, J. (2008). Design of an electrochemical cell making syngas (CO+ H2) from C O2 and H2 O reduction at room temperature. J. Electrochem. Soc. *155*, 42–49.

Dinh, C.T., Burdyny, T., Kibria, G., Seifitokaldani, A., Gabardo, C.M., PelayoGarcía De Arquer, F., Kiani, A., Edwards, J.P., De Luna, P., Bushuyev, O.S., et al. (2018). CO2 electroreduction to ethylene via hydroxide-mediated copper catalysis at an abrupt interface. Science *360*, 783–787.

Dufek, E.J., Lister, T.E., and McIlwain, M.E. (2012). Influence of electrolytes and membranes on cell operation for Syn-Gas Production. Electrochem.Solid StateLett. *15*, 100–102.

Gabardo, C.M., O'Brien, C.P., Edwards, J.P., McCallum, C., Xu, Y., Dinh, C.T., Li, J., Sargent, E.H., and Sinton, D. (2019). Continuous carbon dioxide electroreduction to concentrated multi-carbon products using a membrane electrode assembly. Joule *3*, 2777–2791.

Gallo, A., Snider, J.L., Sokaras, D., Nordlund, D., Kroll, T., Ogasawara, H., Kovarik, L., Duyar, M.S., and Jaramillo, T.F. (2019). Ni5Ga3 catalysts for CO2 reduction to methanol: exploring the role of Ga surface oxidation/reduction on catalytic activity. Appl. Catal. B Environ. 118369, https://doi.org/10.1016/j.apcatb.2019.118369.

García de Arquer, F.P., Dinh, C.-T., Ozden, A., Wicks, J., McCallum, C., Kirmani, A.R., Nam, D.-H., Gabardo, C., Seifitokaldani, A., Wang, X., et al. (2020). CO 2 electrolysis to multicarbon products at activities greater than 1 A cm −2. Science *367*, 661–666.

Ge, N., Banerjee, R., Muirhead, D., Lee, J., Liu, H., Shrestha, P., Wong, A.K.C., Jankovic, J., Tam, M., Susac, D., et al. (2019). Membrane dehydration with increasing current density at high inlet gas relative humidity in polymer electrolyte membrane fuel cells. J. Power Sources *422*, 163–174.

Kuhl, K.P., Cave, E.R., Abram, D.N., and Jaramillo, T.F. (2012). New insights into the electrochemical reduction of carbon dioxide on metallic copper surfaces. Energy Environ. Sci. *5*, 7050–7059.

Lee, C., Lee, J.K., Zhao, B., Fahy, K.F., and Bazylak, A. (2020). Transient gas distribution in porous transport layers of polymer electrolyte membrane electrolyzers. J. Electrochem. Soc. *167*, 024508.

Li, F., Thevenon, A., Rosas-hernández, A., Wang, Z., Li, Y., Gabardo, C.M., Ozden, A., Dinh, C.T., Li, J., Wang, Y., et al. (2020). Molecular tuning of CO_2-to-ethylene conversion*577* (Nature), pp. 509–513.

Liu, K., Smith, W.A., and Burdyny, T. (2019). Introductory guide to assembling and operating gas diffusion electrodes for electrochemical CO 2 reduction. ACS EnergyLett *4*, 639–643.

Ma, M., Clark, E.L., Therkildsen, K.T., Dalsgaard, S., Chorkendorff, I., and Seger, B. (2020). Insights into the carbon balance for CO2 electroreduction on Cu using gas diffusion electrode reactor designs. Energy Environ. Sci. https://doi.org/10.1039/D0EE00047G.

Martín, A.J., Larrazábal, G.O., and Pérez-Ramírez, J. (2015). Towards sustainable fuels and chemicals through the electrochemical reduction of CO2: lessons from water electrolysis. Green.Chem. *17*, 5114–5130.

Nwabara, U.O., Cofell, E.R., Verma, S., Negro, E., and Kenis, P.J.A. (2019). Durable cathodes and electrolyzers for the efficient aqueous electrochemical reduction of CO2. ChemSusChem. https://doi.org/10.1002/cssc.201902933.

Peters, G.P., Andrew, R.M., Canadell, J.G., Friedlingstein, P., Jackson, R.B., Korsbakken, J.I., Le Quéré, C., and Peregon, A. (2020). Carbon dioxide emissions continue to grow amidst slowly emerging climate policies. Nat. Clim. Chang. *10*, 3–6.

Schulz, K.G., Riebesell, U., Rost, B., Thoms, S., and Zeebe, R.E. (2006). Determination of the rate constants for the carbon dioxide to bicarbonate inter-conversion in pH-buffered seawater systems. Mar. Chem. *100*, 53–65.

Sen, S., Brown, S.M., Leonard, M.L., and Brushett, F.R. (2019). Electroreduction of carbon dioxide to formate at high current densities using tin and tin oxide gas diffusion electrodes. J. Appl. Electrochem. *49*, 917–928.

Singh, M.R., Goodpaster, J.D., Weber, A.Z., Head-Gordon, M., and Bell, A.T. (2017). Mechanistic insights into electrochemical reduction of CO2 over Ag using density functional theory and transport models. Proc. Natl. Acad. Sci. U S A *114*, E8812–E8821.

Smith, W.A., Burdyny, T., Vermaas, D.A., and Geerlings, H. (2019). Pathways to industrial-scale fuel out of thin air from CO2 electrolysis. Joule *3*, 1822–1834.

Verma, S., Hamasaki, Y., Kim, C., Huang, W., Lu, S., Jhong, H.R.M., Gewirth, A.A., Fujigaya, T., Nakashima, N., and Kenis, P.J.A. (2018). Insights into the low overpotentialelectroreduction of CO2 to CO on a supported gold catalyst in an alkaline flow electrolyzer. ACS EnergyLett *3*, 193–198.

Vermaas, D.A., and Smith, W.A. (2016). Synergistic electrochemical CO2 reduction and water oxidation with a bipolar membrane. ACS EnergyLett. *1*, 1143–1148.

Weekes, D.M., Salvatore, D.A., Reyes, A., Huang, A., and Berlinguette, C.P. (2018). Electrolytic CO 2 reduction in a flow cell. Acc. Chem. Res. *51*, 910–918.

Wysokinski, T.W., Chapman, D., Adams, G., Renier, M., Suortti, P., and Thomlinson, W. (2013). Beamlines of the biomedical imaging and therapy facility at the Canadian Light Source - Part 2. J. Phys. Conf. Ser. *425*, 72013.

York, R. (2012). Do alternative energy sources displace fossil fuels? Nat. Clim. Chang. *2*, 441–443.

Zheng, T., Jiang, K., Ta, N., Hu, Y., Zeng, J., Liu, J., and Wang, H. (2019). Large-scale and highly selective CO2 electrocatalytic reduction on nickel single-atom catalyst. Joule *3*, 265–278.

iScience, Volume *23*

Supplemental Information

Bubble Formation in the Electrolyte Triggers Voltage Instability in CO_2 Electrolyzers

ChungHyuk Lee, Benzhong Zhao, Jason K. Lee, Kieran F. Fahy, Kevin Krause, and Aimy Bazylak

TRANSPARENT METHODS

Cell Assembly and Operation

A custom single-cell CO_2 electrolyzer was designed to enhance liquid, gas, and solid contrast via X-ray radiography. The active area of the membrane-electrode assembly (MEA) was 5 mm along the direction traversed by the X-ray beam and 16 mm wide. For the cathode compartment, we used a commercial silver-based cathode gas diffusion electrode (Oxag, Gaskatel mbH). The electrolyte chamber was 2.3 mm thick, 6 mm along the direction traversed by the X-ray beam, and 17 mm wide. The chamber was 3D-printed with polycarbonate and was packed with 11 sheets of high-density polyethylene mesh (porosity of 0.65) to provide structural support to the membrane and the GDE. We used a Nafion HP membrane with an anode iridium catalyst (1.0 mg/cm_2) coated on one side, and a commercial titanium porous transport layer (PTL) (1100 Series, Mott Corp.) was used as the anode PTL. The MEA was placed between two titanium flow fields that were coated with 0.5 μm thick gold and 2.5 μm thick platinum to avoid the formation of oxide layers on the titanium surface. The flow fields featured 16 parallel flow channels (0.5 mm wide and 0.5 mm deep) and the channels were separated by lands (0.5 mm wide). We supplied 10 mL/min of deionized water (fresh) to the anode flow channels, and 6 mL/min of electrolyte (recirculated) to the electrolyte chamber using a peristaltic pump (Masterflex L/S precision variable-speed console drive, Cole-Parmer). We placed pulse dampeners downstream of the pump to provide constant flow to the electrolyzer. We supplied 100 mL/min of dry CO_2 gas to the cathode flow channels via a mass flowmeter (5000 sccm Elastomer-Sealed Digital Mass Flow Controller, MKS Instruments).

The experiments were conducted at room temperature, and the electrolyzer was galvanostatically operated using a potentiostat (Gamry Reference 3000, Gamry Instruments). We operated the electrolyzer at 6 current densities: 5, 10, 20, 40, 60, and 80 mA/cm$_2$, and each current density was held for 25 min. In between each current density, the electrolyzer was operated at open circuit voltage for 10 min to allow for bubble removal prior to the subsequent current density step. The resulting cell voltage was recorded every second.

Synchrotron X-ray Imaging Setup

The custom CO_2 electrolyzer cell was imaged at the Biomedical Imaging and Therapy Wiggler Insertion Device beamline at the Canadian Light Source Inc. in Saskatoon, Canada (Wysokinski et al., 2013). Incident X-ray (photon energy level of 30 keV) traversed through the electrolyte chamber. We used a complementary metal-oxide-semiconductor camera (C11440-22CU, Hamamatsu) to capture the images, and the resulting pixel resolution and temporal resolution were 6.5 μm and 1 fps. Two types of images were captured: a reference image (captured when the electrolyte chamber was assumed to be fully saturated with the liquid electrolyte, and current was not applied), and operational images (captured during operation).

All images were processed using the following procedure: dark-field correction, beam intensity correction, and Beer-Lambert law. For the dark-field correction step, we subtracted all images by a dark-field image (image obtained without X-ray beam) to remove all noise generated from the camera hardware (Ge et al., 2016). Beam intensity correction was performed to remove the effects of decay in beam intensity over time (Ge et al., 2016), and the detail of this correction algorithm

is reported in Ge et al. (Ge et al., 2016). After dark-field and beam intensity corrections, we applied Beer-Lambert law to quantify the volumetric changes in the electrolyte content from the reference state in each pixel:

$$V = \frac{1}{\mu} ln\left(\frac{I_{op}}{I_{ref}}\right) x^2 \quad \text{(S.1)}$$

where μ is the attenuation coefficient of the electrolyte [cm^{-1}], I_{op} and I_{ref} are the intensities of operational and reference images, respectively [-], and x is the spatial resolution [6.5 μm]. The attenuation coefficient of the electrolyte was calibrated by imaging known volumes of the electrolyte (0.5 M) (μ = 0.40 cm^{-1}) (Fig. S1). We used an average of 100 reference images to calculate I_{ref}. Then, the gas saturation (S) was determined as follows:

$$S = \frac{V}{V_P} \quad \text{(S.2)}$$

where V_p is the total volume of pores [m^3].

FIGURE LEGENDS

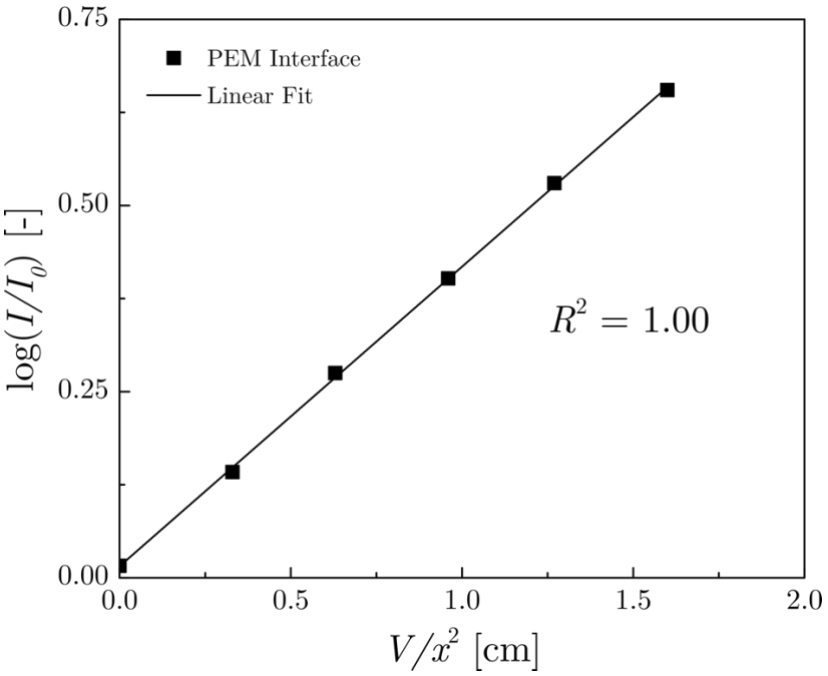

Figure S.1. Related to Fig. 2. Calibration results for determining the attenuation coefficient of $KHCO_3$ (0.5M). The attenuation coefficient was used to quantify the gas volume in the electrolyte chamber, shown in Fig. 2.

REFERENCES

Ge, N., Chevalier, S., Hinebaugh, J., Yip, R., Lee, J., Antonacci, P., Kotaka, T., Tabuchi, Y., Bazylak, A., (2016). Calibrating the X-ray attenuation of liquid water and correcting sample movement artefacts during in operando synchrotron X-ray radiographic imaging of polymer electrolyte membrane fuel cells. J. Synchrotron Radiat. 23, 590–599.

Wysokinski, T.W., Chapman, D., Adams, G., Renier, M., Suortti, P., Thomlinson, W., (2013). Beamlines of the biomedical imaging and therapy facility at the Canadian Light Source - Part 2. J. Phys. Conf. Ser. 425. https://doi.org/10.1088/1742-6596/425/7/072013